

Chapter 14

Photoemission from Nanomaterials in Strong Few-Cycle Laser Fields

Qingcao Liu, Philipp Rupp, Benjamin Förg, Johannes Schötz, Frederik Süßmann, William Okell, Johannes Passig, Josef Tiggesbäumker, Karl-Heinz Meiwes-Broer, Lennart Seiffert, Thomas Fennel, Eckart Rühl, Michael Förster, Peter Hommelhoff, Sergey Zherebtsov, and Matthias F. Kling

Abstract The application of ultra-short waveform-controlled laser fields to nanostructured materials enables the generation of localized near-fields with well-defined spatiotemporal field evolution. The optical fields that can be tailored on sub-wavelength spatial and attosecond temporal scales have a high potential for the control of ultrafast processes at the nanoscale, with important implications for laser-driven electron acceleration, extreme ultraviolet (XUV) light generation, and nanoscale electronics operating at optical frequencies.

Q. Liu (✉) • P. Rupp • B. Förg • J. Schötz • F. Süßmann • S. Zherebtsov • M.F. Kling (✉)
Department of Physics, LMU Munich, Am Coulombwall 1, D-85748 Garching, Germany

Max Planck Institute of Quantum Optics, Hans-Kopfermann-Str. 1, D-85748 Garching, Germany
e-mail: liuqingcao@gmail.com; matthias.kling@mpq.mpg.de

W. Okell

Max Planck Institute of Quantum Optics, Hans-Kopfermann-Str. 1, D-85748 Garching, Germany

J. Passig • J. Tiggesbäumker • K.-H. Meiwes-Broer • L. Seiffert • T. Fennel

Institut für Physik, Universität Rostock, D-18051 Rostock, Germany

E. Rühl

Physical Chemistry, Freie Universität Berlin, Takustr. 3, D-14195 Berlin, Germany

M. Förster • P. Hommelhoff

Max Planck Institute of Quantum Optics, Hans-Kopfermann-Str. 1, D-85748 Garching, Germany

Department of Physics, Friedrich-Alexander University Erlangen-Nürnberg (FAU), Staudtstrasse 1, D-91058 Erlangen, Germany

14.1 Waveform-Control of Strong Field Dynamics in the Near-Field of Isolated Nanoparticles

14.1.1 Introduction

Field localization by non-resonantly excited nanostructures opens new avenues in strong-field physics with optical fields that can be tailored on sub-wavelength spatial and attosecond temporal scales. Enhanced strong-field electron acceleration in nanolocalized fields has been observed in isolated dielectric nanospheres, metal nanotips, and surface based nanostructures. Here, we present our results on strongfield-induced waveform-controlled dynamics in isolated nanoparticles.

14.1.2 Imaging of Laser-Induced Electron Emission from Isolated Nanoparticles

In experiments exploring the waveform control of electron photoemission from isolated nanoparticles, few-cycle laser fields with controlled carrier-envelope phase (CEP) were employed [1, 2]. Few-cycle laser pulses of ~ 4.5 fs duration centered at 720 nm were generated from the output of an amplified laser system (25 fs pulse duration, 790 nm central wavelength) [3] that was spectrally broadened in a capillary filled with 2.8 bar Ne gas, and compressed by a chirped mirror compressor. For each laser pulse the CEP was measured with a stereo-ATI phasemeter [4, 5] using a small fraction of the laser beam ($\sim 15\%$). The main part of the beam was focused into the center of the electrostatic optics of a velocity-map imaging (VMI) detector, where it intersected a nanoparticle beam (see Fig. 14.1a). The electron emission distribution was projected onto a microchannel plate (MCP) and phosphor screen assembly, and the image on the phosphor screen was recorded by a high-speed CMOS camera at the full repetition rate of the laser (1 kHz) [6]. Acquisition of single-shot images at these high rates was achieved by only storing pixels whose brightness exceeded a threshold level. The SiO₂ nanospheres were prepared by using wet chemistry methods [7, 8] for producing spheres with diameters in the range 50–550 nm and polydispersity of less than 10 % [1, 9] (e.g. Fig. 14.1b). The isolated nanospheres were delivered into the interaction region by injection of the nanospheres suspension into a carrier gas, evaporation of the solvent (ethanol), focusing of the nanospheres stream with an aerodynamic lens, and differential pumping of the carrier gas.

With the current efficiency of the nanoparticle source the particle density in the interaction region is limited and typically only one out of a few (5–10) frames contains nanoparticle signal. As the number of electrons emitted from the nanoparticles is significantly larger than the electron emission from the residual gas, single-shot detection allows significant improvement of the signal-to-noise ratio by selecting only those frames that contain nanoparticle signal. Figure 14.1c shows histograms

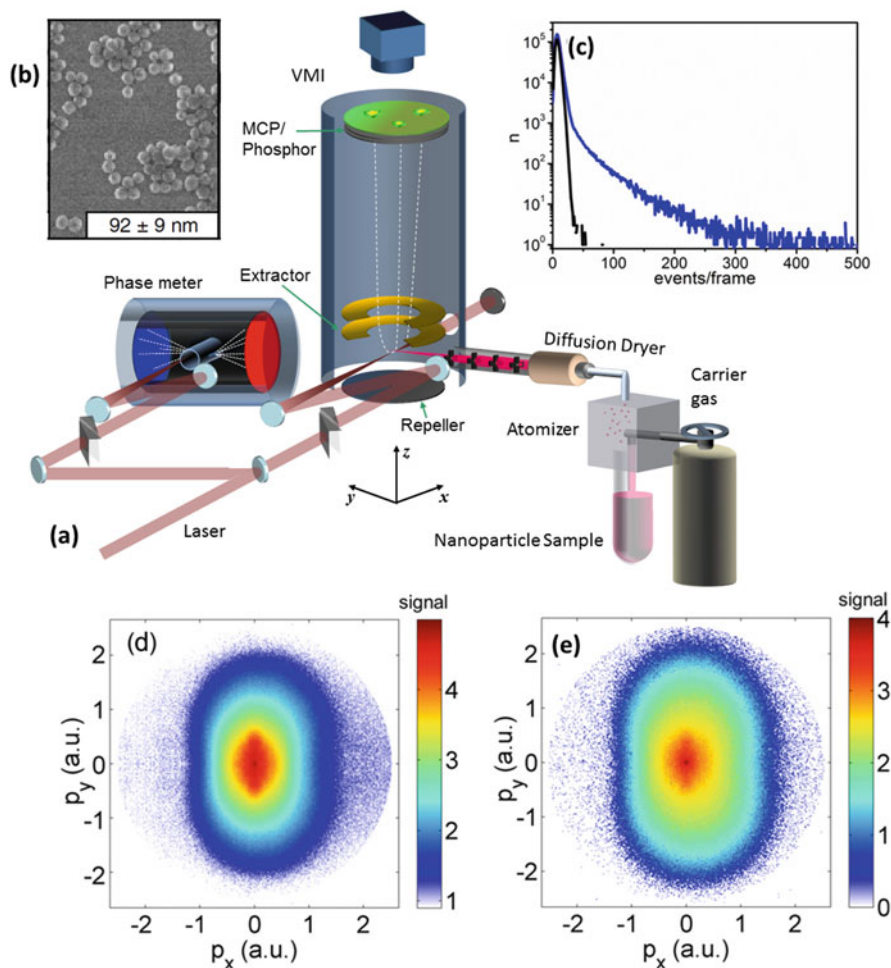


Fig. 14.1 (a) Schematic of the VMI setup with an aerodynamic nanoparticle source and single-shot phasemeter. The polarization of the laser was in the plane of the detector. (b) TEM image of 92 nm diameter SiO₂ nanospheres. (c) Histograms of the number of events per frame obtained from the solvent ethanol only (*black line*) and SiO₂ nanospheres in ethanol (*blue line*) measurements. (d, e) CEP-averaged VMI images (log color scale) obtained from measurements with a suspension of SiO₂ nanospheres in ethanol. The image in (d) is the average over all the frames, and the image in (e) is the average over only the frames containing more than 30 events

of the number of events per frame for the ethanol-only (black) and suspension of nanoparticles in ethanol (blue) measurements. While the ethanol-only measurement signal is concentrated at low event numbers, in nanoparticle measurements many frames contain a much higher number of events. Figure 14.1d, e illustrate efficient suppression of the background signal by neglecting the frames with low event numbers.

14.1.3 Waveform-Controlled Electron Near-Field Acceleration

Figure 14.2a, b show typical results for VMI of waveform-controlled electron photoemission from 95 nm diameter SiO₂ nanoparticles illuminated with CEP-controlled few-cycle laser fields. The electron momentum distribution has an elliptical shape and is elongated along the polarization direction (p_y axis) (Fig. 14.2a). To quantify the CEP dependence of the directional emission an asymmetry parameter $A(p_y, \varphi) = (P_{up}(p_y, \varphi) - P_{down}(p_y, \varphi)) / (P_{up}(p_y, \varphi) + P_{down}(p_y, \varphi))$ was plotted as a function of the momentum along polarization axis (p_y) and CEP (φ). Here $P_{up}(p_y, \varphi)$ and $P_{down}(p_y, \varphi)$ are the angle-integrated electron yields (within $[-25^\circ, +25^\circ]$ angular range) in the up (positive p_y momentum) and down (negative p_y momentum) directions (Fig. 14.2b). The cutoff of the momentum map is in agreement with the cutoff of the CEP-dependent electron emission and is at about $50 U_p$, where U_p is the ponderomotive potential of an electron in the driving laser field. For the studied intensity range $(1-4.5) \times 10^{13}$ W/cm² the measurements show a nearly linear intensity dependence of the cutoff energy with an average scaled cutoff of about $53.0 U_p$ (Fig. 14.2e). The measured cutoff energy is much higher than what is expected for the classical atomic emission in a dielectrically enhanced field near a SiO₂ nanosphere (cutoff of $\sim 24 U_p$). The maximum asymmetry phase φ_{max} increases with the laser intensity (except the lowest intensity point) (Fig. 14.2f).

The mechanism of the enhanced electron acceleration was analyzed with quasi-classical trajectory-based simulations using the Meanfield Monte-Carlo model developed in the group of one of the authors (Th. Fennel) [2]. Results of these calculations performed for the same parameters as in the experiment are presented in Fig. 14.2c–f. The simulations reproduce the main features of the experiment such as overall shape of the momentum and asymmetry maps as well as the cutoff value. The simulation model explained these effects through many-particle charge interaction of ionized electrons and positively charged ions in the nanoparticle. The charge interaction can be decomposed into a short-range nonlinear surface potential due to self-consistent electron motion in the local field and a long-range potential due to ionization. While the long-range potential traps the low-energy direct electrons, both components contribute to the backscattered electron acceleration. Persistence of the observed CEP controlled electron photoemission over a wide intensity range indicates robustness of the near-field induced electron recollision process even at laser intensities when the multi-particle nonlinear response of the system becomes significant. The simulation shows a good agreement with the experiment except for the lowest intensity point (Fig. 14.2e, f). The discrepancy at the lowest intensity can be ascribed to the deviation of the initial ionization mechanism from the instantaneous tunneling assumed in the model.

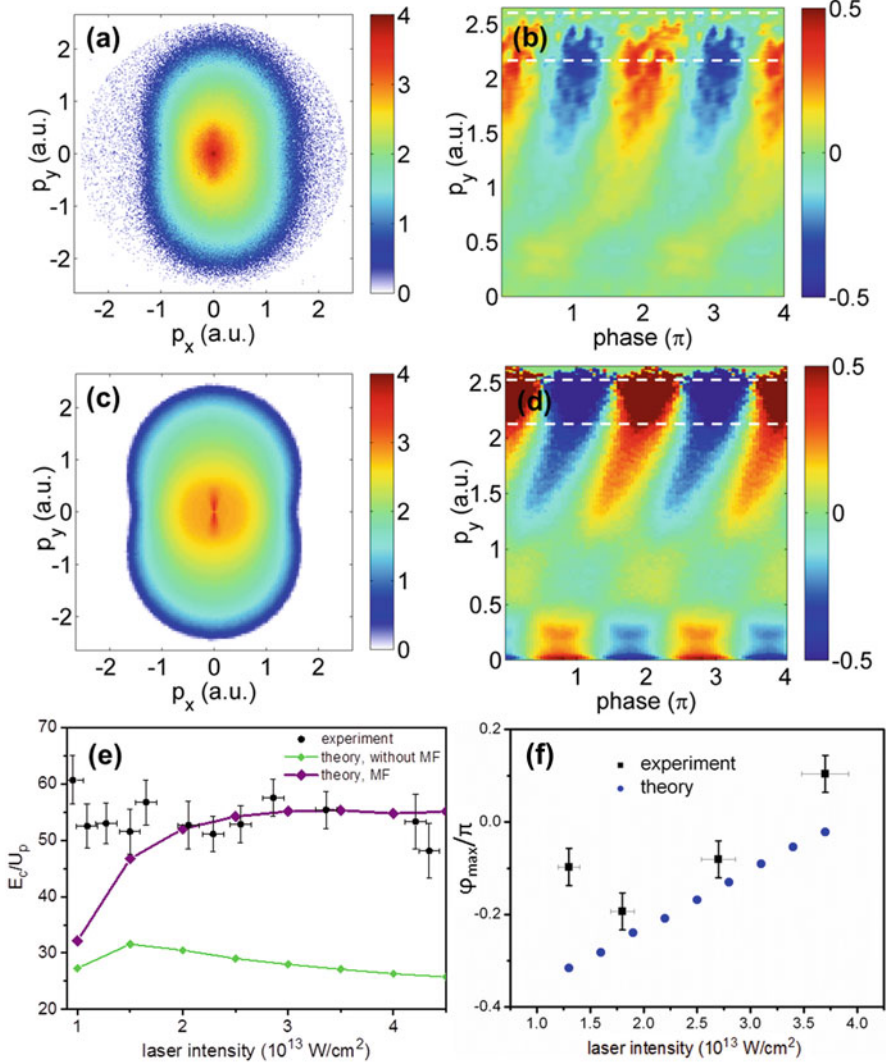


Fig. 14.2 (a) Photoelectron momentum map (projected along p_z) averaged over the CEP (log color scale) and (b) asymmetry of the electron emission as a function of the electron momentum and the CEP measured for 95 nm SiO₂ nanoparticles at 3.7×10^{13} W/cm². (c, d) Photoelectron momentum and asymmetry map calculated for the same parameters as in (a, b). (e) Intensity dependence of the electron emission cutoff in terms of U_p measured in SiO₂ nanoparticles (filled black circles) and results of the model simulations without mean field (green line with filled circles) and including mean field contribution (purple line with filled circles). (f) Dependence of the CEPs at the maximum asymmetry φ_{max} of the electron emission from SiO₂ nanoparticles of 95 nm diameter on the laser intensity measured (black boxes) and calculated (blue filled circles). To obtain φ_{max} the asymmetry maps were integrated over p_y in the cutoff region (indicated by white dashed lines in (b, d)) and fitted with a function $f(\varphi_{max}) = A * \cos(\varphi_{CEP} - \varphi_{max})$.

14.1.4 *Effect of Field-Propagation Deformation on Electron Photoemission from Isolated Nanospheres*

Local field sensitivity of the near-field-driven electron photoemission prompted further work on tailoring near-fields for control of strong-field-induced electron dynamics. In the first proof of principle experiment we employed isolated nanospheres of different diameters for the generation of near-fields with adjustable polarization and spatial characteristics. Isolated nanospheres have the advantage that their linear near-field properties can be analytically described. The linear response of a sphere can be accurately described by the Mie solution [10] and for a given refractive index, it is determined by the sphere diameter d and the central wavelength of the excitation field λ through the dimensionless parameter $\rho = \pi d/\lambda$. For spheres much smaller than the excitation wavelength ($\rho \ll 1$) the field distribution exhibits quasi-static dipole character with the poles aligned along the polarization vector. For large sphere diameters ($\rho \gg 1$) excitation of higher order modes results in a significant shift of the region of maximal field enhancement in the field propagation direction. Figure 14.3a shows the near-field distribution of the radial electric field as predicted by Mie theory for 100 and 550 nm diameter SiO₂ particles. For large nanospheres the field propagation also induces a nontrivial elliptical local field due to a phase difference between the radial and tangential components (Fig. 14.3a). The CEP-modulation amplitude maps of SiO₂ nanoparticles for diameters of 95 nm and 400 nm are shown in Fig. 14.3b and c, respectively. The shape of the amplitude maps is as expected dipolar without a noticeable asymmetry around $p_x = 0$. A bending of the momentum distribution towards the laser propagation axis can be observed for $d = 400$ nm.

We utilized isolated SiO₂ nanospheres of different diameters ($d = 50$ – 550 nm) to study the size-dependence of the near-field deformation on the strong field induced photoemission. The effect of field propagation on the phase controlled electron photoemission is illustrated in Fig. 14.4a, b. For this energetic electron emission near the cutoff, the yield is presented as a function of emission angle and CEP. Comparison of the electron emission for nanospheres with diameters between 95 and 550 nm (Fig. 14.4e, f) shows concentration of the energetic emission within a narrow angular range, and a pronounced CEP dependence that is in phase for small and large particles. While for the small nanospheres the signal is concentrated along the polarization vector, for the large nanospheres the emission is tilted towards the propagation direction, reflecting a field-propagation-induced change in the near-field distribution. For modeling the experiment the quasi-classical Monte-Carlo trajectory-based model was extended to take into account the field deformations by means of the Mie solution (Mean-Field Mie Monte-Carlo (M³C)) [10, 11]. The model simulations (Fig. 14.4c, d) reproduce the main experimental results indicating that all major effects contributing to the electron acceleration are included in the model. The size dependence of the critical emission parameters is illustrated in Fig. 14.4e, f. The systematic tunability of the photoemission direction and CEP

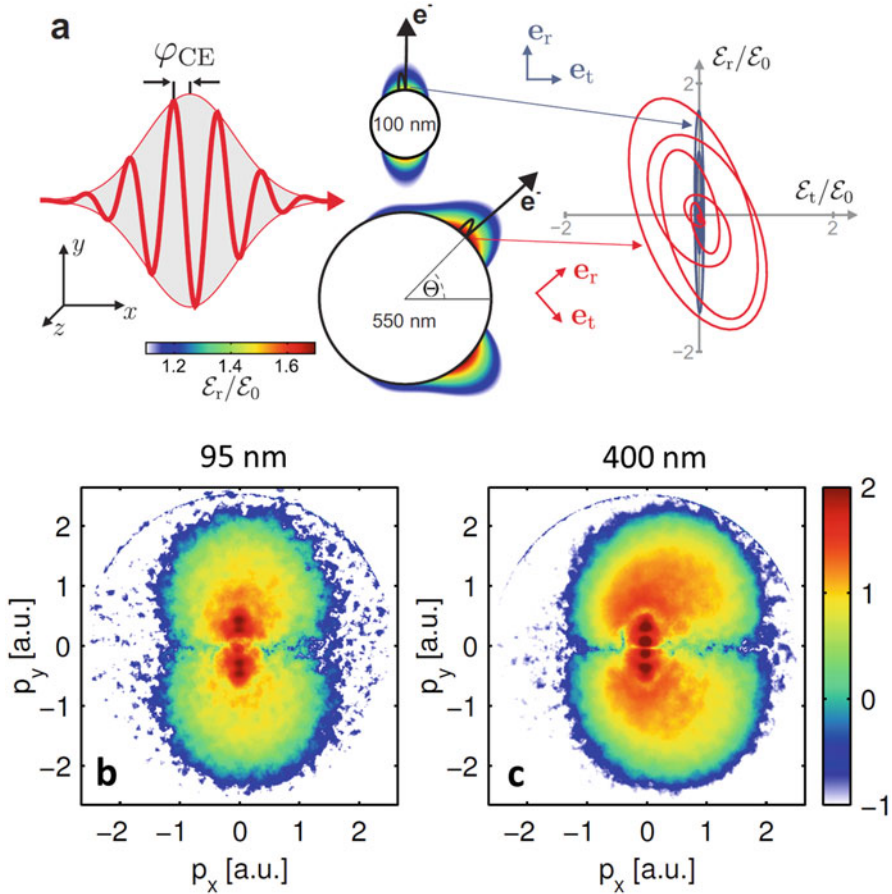


Fig. 14.3 (a) Peak radial field enhancement in the x - y plane at $z = 0$ obtained by Mie solution for SiO_2 spheres illuminated with a 4 fs linear polarized laser pulse centered at 720 nm and a CEP of $\varphi_{CEP} = 0$ (left). Field evolution in the local reference frame at the points of maximum field enhancement (right). (b, c) Amplitude of the CEP-dependent part of the electron emission obtained from measurements of SiO_2 nanoparticles of 95 nm (b) and 400 nm (c) diameters (logarithmic scale, arbitrary units)

dependence of the electron emission indicates a robust attosecond control over the recollision process in sculpted near fields. Quantitative analysis of different many-particle contributions to the acceleration process (Fig. 14.4g) shows a weak size-dependence of the short-range nonlinear surface potential that can be explained by the local character of this potential. On the other hand the contribution from the long-range space-charge repulsion increases strongly with the particle size, indicating its sensitivity to the full electron distribution.

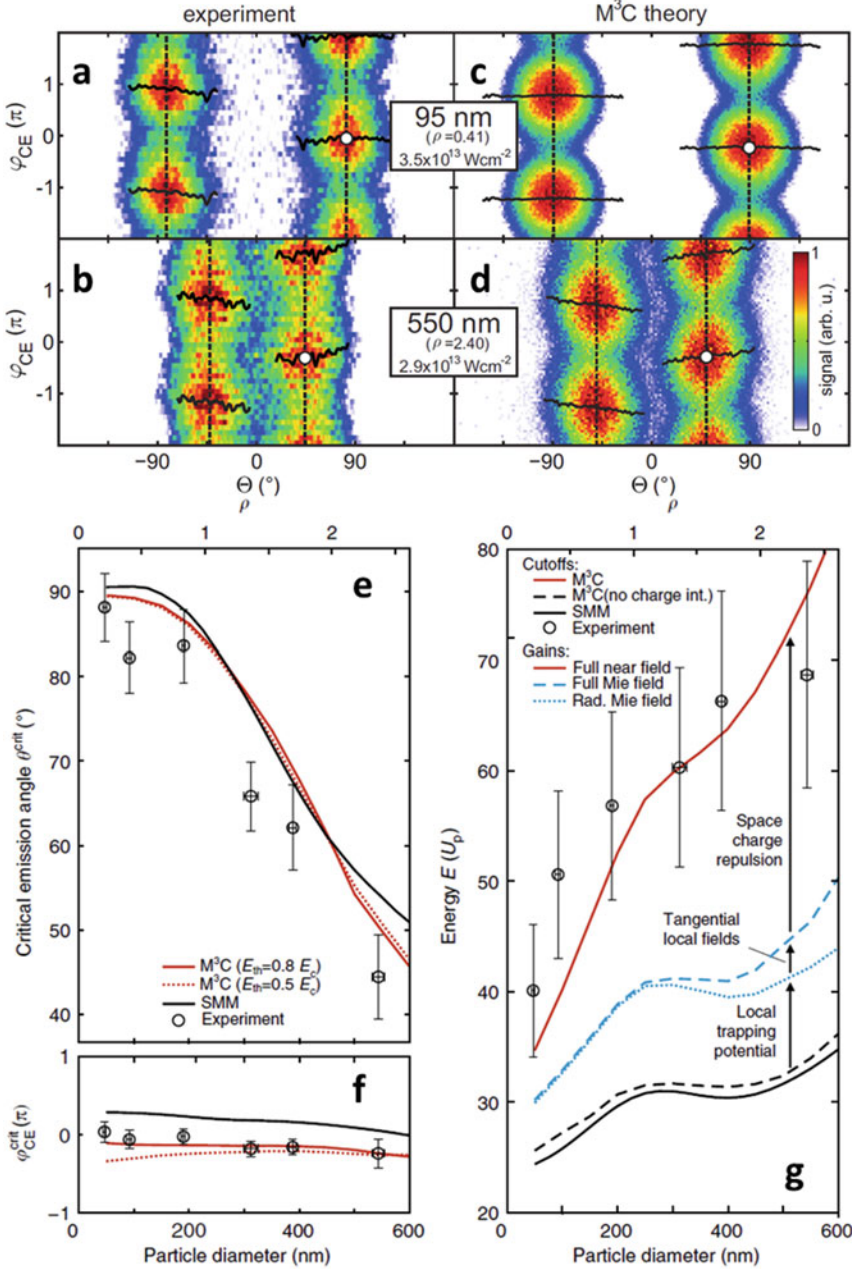


Fig. 14.4 (a–d) Measured (a, b) and simulated (c, d) angle and CEP-resolved electron yields of energetic electrons near cutoff. The white dots indicate CEP values φ_{CEP}^{crit} and emission angles θ^{crit} of maximum upward emission. (e, f, g) Particle size dependence of the critical emission angle (e), critical phase (f), and cutoff energies (g). The symbols and lines indicate measured and calculated parameters. The Simple Man’s Model (SMM) is described in details in Refs. [10, 11]

14.1.5 Nonlinear Regime Near Optical Breakdown

The work presented in the previous section is focused on the response of nanoparticles excited by relatively moderate laser fields in the regime where the optical response of the material can still be assumed linear. The response of solid materials at laser intensities close to the damage threshold has been a subject of both experimental and theoretical studies [12, 13]. These studies are motivated by interest in the fundamental laser-matter interaction, and by prospective applications in material processing, and ultrafast computation. As typical time scales for energy transfer in solids range from fs for electron-electron interaction to ps for electron-phonon and tens of ps for phonon-phonon interaction, the laser energy deposition process strongly depends on the laser pulse duration. For pulse durations of tens of ps the melting process occurs during the interaction of the laser pulse with the solid. For sub-picosecond laser pulses the ultrafast deposition of energy into the electron system leads to a local Coulomb explosion of ions (laser ablation) [14]. For pulses longer than 100 fs the creation of free electrons is attributed mainly to avalanche ionization [14, 15]. For pulses of 5 fs duration the ionization process is dominated by multi-photon and tunnel ionization, and peak intensities exceeding 10^{14} W/cm² are necessary to induce optical breakdown [16].

Because the detection range of the electron kinetic energies of the VMI spectrometer used in the previous studies is limited to about 100 eV, we used a stereo-TOF spectrometer (Fig. 14.5a). Isolated nanoparticles are especially well suited for these

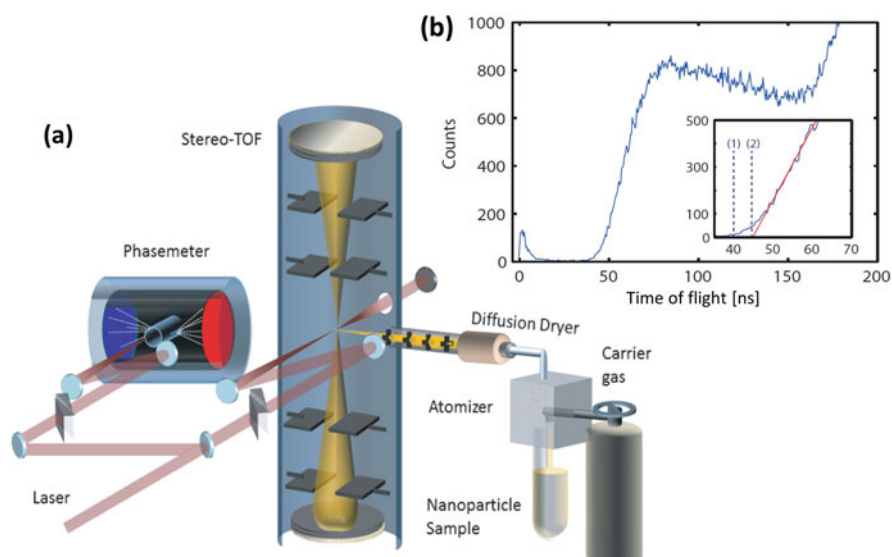


Fig. 14.5 (a) Schematic of the single-shot stereo-TOF setup for high intensity waveform controlled photoemission from isolated nanoparticles. (b) Typical TOF spectrum obtained from SiO₂ nanoparticles excited by a few-cycle laser field. The inset shows the two methods for determining the cutoff

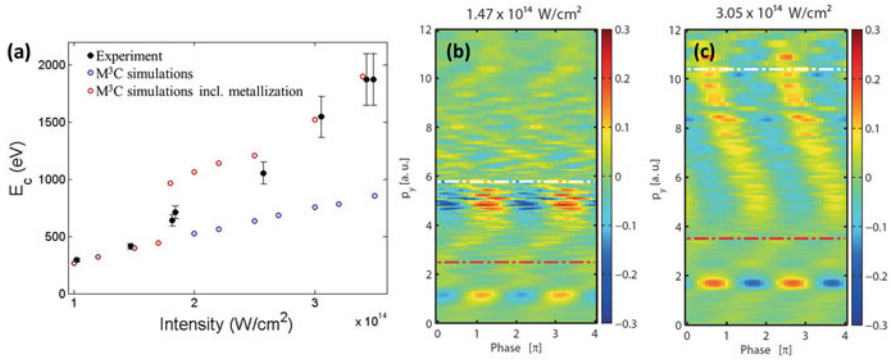


Fig. 14.6 (a) Intensity dependence of the electron emission cutoff measured in SiO₂ nanoparticles (filled black circles) and results of the M³C model simulations for SiO₂ without metallization (open blue circles) and including metallization (open red circles). (b, c) Asymmetry maps obtained from the measurements of SiO₂ nanoparticles at the laser intensities indicated above the corresponding panels. The cutoff momentum obtained from the TOF spectrum is indicated for the nanoparticle (white dashed line) as well as for the reference scan (red dashed line)

studies as the target is replaced for each laser shot. A typical TOF spectrum is presented in Fig. 14.5b. The sharp peak at small delays is induced by light scattering (and possibly light emission) from the nanoparticles and was used to calibrate the time-zero of the TOF trace.

The results of intensity-dependent measurements are presented in Fig. 14.6. For intensities up to $\sim 1.5 \times 10^{14} \text{ W}/\text{cm}^2$ the cutoff energies are nearly linear with the intensity of the incident laser field and are in agreement with the low intensity limit of about $50 U_p$ obtained from VMI measurements. At higher laser intensities the emission cutoff in terms of U_p monotonically increases and reaches $100 U_p$ at an intensity of $\sim 3.5 \times 10^{14} \text{ W}/\text{cm}^2$ (Fig. 14.6a). The M³C simulations reproduce the experiment at intensities below $\sim 1.5 \times 10^{14} \text{ W}/\text{cm}^2$ while they significantly underestimate the cutoff energies at higher laser intensities. This observation together with a change of the asymmetry map shape above the critical intensity (Fig. 14.6b, c) indicates an onset of nonlinear response of the material that is not included in the model. It was shown recently that electric polarizability and electronic structure of SiO₂ can be manipulated reversibly with few-cycle laser fields at similar laser intensities [17]. To account for the nonlinear process in SiO₂ we simulated the high-intensity response of the nanoparticle by switching the permittivity of the material to that of Au, as the field intensities at the surface of the nanoparticle reach $\sim 1.5 \times 10^{14} \text{ W}/\text{cm}^2$. The modified (and still crude) model is in better agreement with the experiment at the highest intensities, while it still requires improvement to correctly describe the transition process at intensities around $1.5 \times 10^{14} \text{ W}/\text{cm}^2$.

14.2 Attosecond Streaking in Nanolocalized Plasmonic Fields

In the waveform-controlled electron emission experiments presented above, reconstruction of the time evolution of the nanoscale near-fields relies to a large extent on model calculations. In contrast, a pump-probe approach provides direct access to the near-field dynamics. So far, ultrafast plasmonic near-fields surrounding nanowires, nanoantennas, and nanotips have been studied using femtosecond pulse characterization techniques [18–22]. By virtue of an enhanced temporal resolution, attosecond streaking promises to yield an even deeper understanding of the collective electron dynamics governing plasmon formation and decay, where transport and interaction effects on sub-optical-cycle timescales are expected to be important. In nano-plasmonic streaking measurements, the plasmonic field is excited by a few-cycle laser pulse incident on the nanostructures and probed by photoemission induced by an attosecond extreme ultraviolet (XUV) pulse with variable delay. The XUV-induced photoelectrons are accelerated by the plasmonic field [23]. From the delay-dependent spectrogram information on the temporal structures of the streaking field and the XUV pulse, as well as the attosecond electron dynamics taking place in and at the nanostructure can be extracted. For streaking in nanolocalized fields, the situation is more complex than in a standard streaking measurement in the gas phase [24] or at a plain macroscopic surface [25–27]. This is because the electron can, under certain conditions, experience the spatial inhomogeneity of the nanolocalized fields [23]. For few-cycle streaking pulses three different regimes of streaking can be identified, distinguished by the ratio of the time it takes an electron to leave the inhomogeneous field t_0 to the streaking field period T and pulse duration t_p [23, 28, 29]. In the “ponderomotive” limit the streaking field pulse duration t_p is much shorter than the time it takes the electron to leave the near-field t_0 ($t_p \ll t_0$) and the electron does not experience any spatial variation of the near-field. This is the same situation as in a standard streaking measurement. In the “instantaneous” limit the electron leaves the localized field within a fraction of the optical cycle T ($t_0 \ll T$). In contrast to conventional, ponderomotive streaking, in the instantaneous regime the electron streaking curve follows the electric field evolution instead of its vector potential. In the intermediate regime the electron traverses the localized field in about one optical oscillation $t_0 \approx T$ and the streaking trace shows a behavior, which lies in-between the two limits.

14.2.1 Attosecond Streaking in the Near-Field of Isolated Nanospheres

Isolated nanospheres can serve as a reference system for tracing plasmonic excitations because their simple shape permits an analytical description of the near-fields. Experimentally, isolated nanoparticles of well-defined size and shape can be introduced into the interaction region by employing aerodynamic lens focusing [1, 2] or optical trapping [30]. These methods allow isolated nanoparticles to be studied without the influence of a substrate or particle-particle interactions.

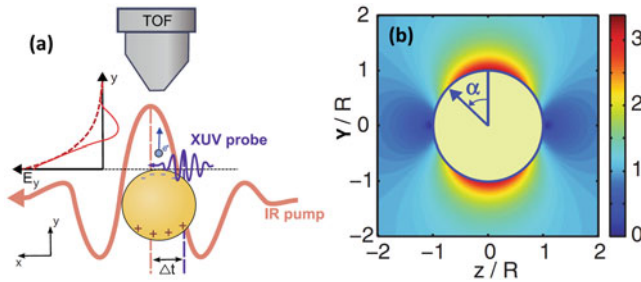


Fig. 14.7 (a) Schematic of an attosecond streaking measurement with an isolated gold nanosphere. (b) Simulation of the amplitude of the field (E_y) distribution at an Au sphere of 100 nm diameter illuminated with a 5 fs pulse centered at 720 nm. The field is normalized to the incident field

Attosecond streaking on isolated gold nanospheres, shown schematically in Fig. 14.7a, was theoretically analyzed to determine what information could be extracted from experiments [31]. The simulations considered plasmonic oscillations excited by a few-cycle NIR laser pulse and probed by photoemission induced by a delayed attosecond XUV pulse. Electron detection was assumed to be performed using a time-of-flight (TOF) spectrometer along the polarization direction of the NIR pulse. To achieve an ultrafast broadband response, an off-resonant 5 fs laser pulse centered at 720 nm was used as the excitation field [31]. The fields around the nanoparticle were calculated by finding the Mie solution at the central laser wavelength. The simulated near-field in Fig. 14.7b exhibits symmetry relative to the polarization vector of the incident field, with the maximum field enhancement at the poles along the polarization vector. The photoemission was initiated by a 250 as XUV pulse (7 eV bandwidth centered at 105 eV). Photoemission from the whole surface facing the TOF was simulated, taking into account XUV attenuation by the nanoparticle. The photoemitted electrons were assumed to have initial velocity vectors parallel to the y -axis (along the TOF axis). The electron initial position is represented by the angle α with respect to the polarization vector of the laser field (Fig. 14.7b). To achieve good statistics approximately 1.5×10^5 trajectories were initialized from the surface at each delay step.

Figure 14.8a, b show streaking curves simulated for different electron initial positions for gold nanoparticles of 10 nm (a) and 100 nm (b) diameter. For the 10 nm diameter nanoparticle the phase shift of the streaking curves relative to the streaking field suggests a gradual change from the ponderomotive regime for electrons emitted at the poles of the particle ($\alpha = 0^\circ$), to a nearly instantaneous regime for electrons emitted at $\alpha = 90^\circ$. This emission position dependence can be attributed to the dipolar character of the near-field, where the spatial extent of the near-field is much larger at the poles of the sphere than at the equator ($\alpha = 90^\circ$). For a much larger 100 nm diameter particle most of the photoemitted electrons experience ponderomotive streaking.

The corresponding streaking spectrograms consisting of contributions from trajectories originating from different parts of the surface are shown in Fig. 14.8c,

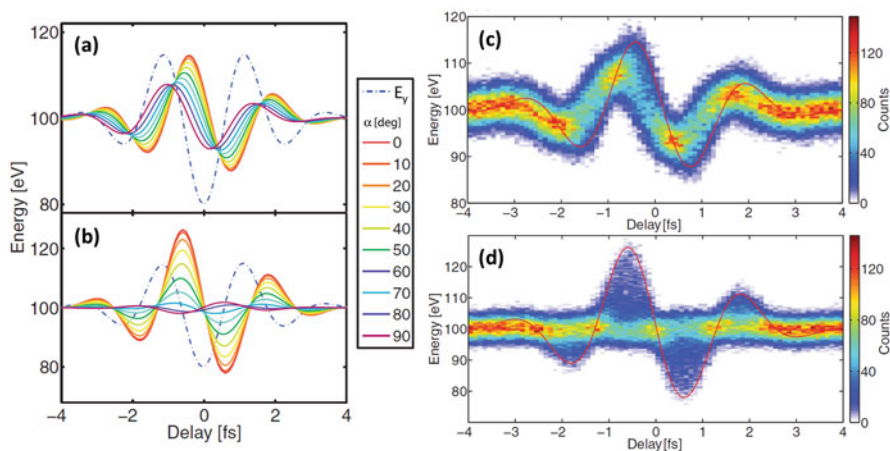


Fig. 14.8 (a, b) Simulated streaking waveform for electrons emitted at different positions on a sphere of 10 nm (a) and 100 nm (b) diameter. The blue dashed lines show the plasmonic near-field at the surface (After [31]). (c, d) Simulated streaking spectrograms for spheres of 10 nm (c) and 100 nm (d) diameter. The red line indicates the streaking curve for electrons emitted at the particle pole

d. In comparison to typical streaking measurements in an atomic gas, streaking on a nanoparticle results in a blurred spectrogram due to different acceleration conditions for electrons emitted from different parts of the nanoparticle. Trajectory analysis shows that the electrons emitted from the poles contribute to the largest energy shifts of the photoelectron spectra (red line in Fig. 14.8c, d). As an analytical description of streaking is generally not available for the complex inhomogeneous fields around nanostructures, numerical simulations combined with appropriate feedback may be employed for the retrieval of the spatiotemporal evolution of the near-fields.

14.2.2 Attosecond Nanoscale Sampling of the Near-Field at Gold Nanotips

Attosecond-resolved experiments with isolated nanoparticles typically require a high XUV photon flux to obtain a practical XUV photoelectron yield due to the limited target density. Nanotips, however, feature relaxed flux requirements due to a higher target density while still maintaining the advantages of studying a single, well-controlled nanostructure. The near-fields at the nanotaper's apex and shank play, exemplarily, a crucial role in the study of strong-field photoemission at nanotapers [32–36] and have recently been examined with femtosecond lasers [37–40]. Here we present our recent results on attosecond near-field retrieval with a tapered gold nanowire using streaking spectroscopy [41].

Figure 14.9a shows a schematic of attosecond nanoplasmonic near-field sampling around a nanotaper. Phase-stabilized few-cycle laser pulses of 4.5 fs duration

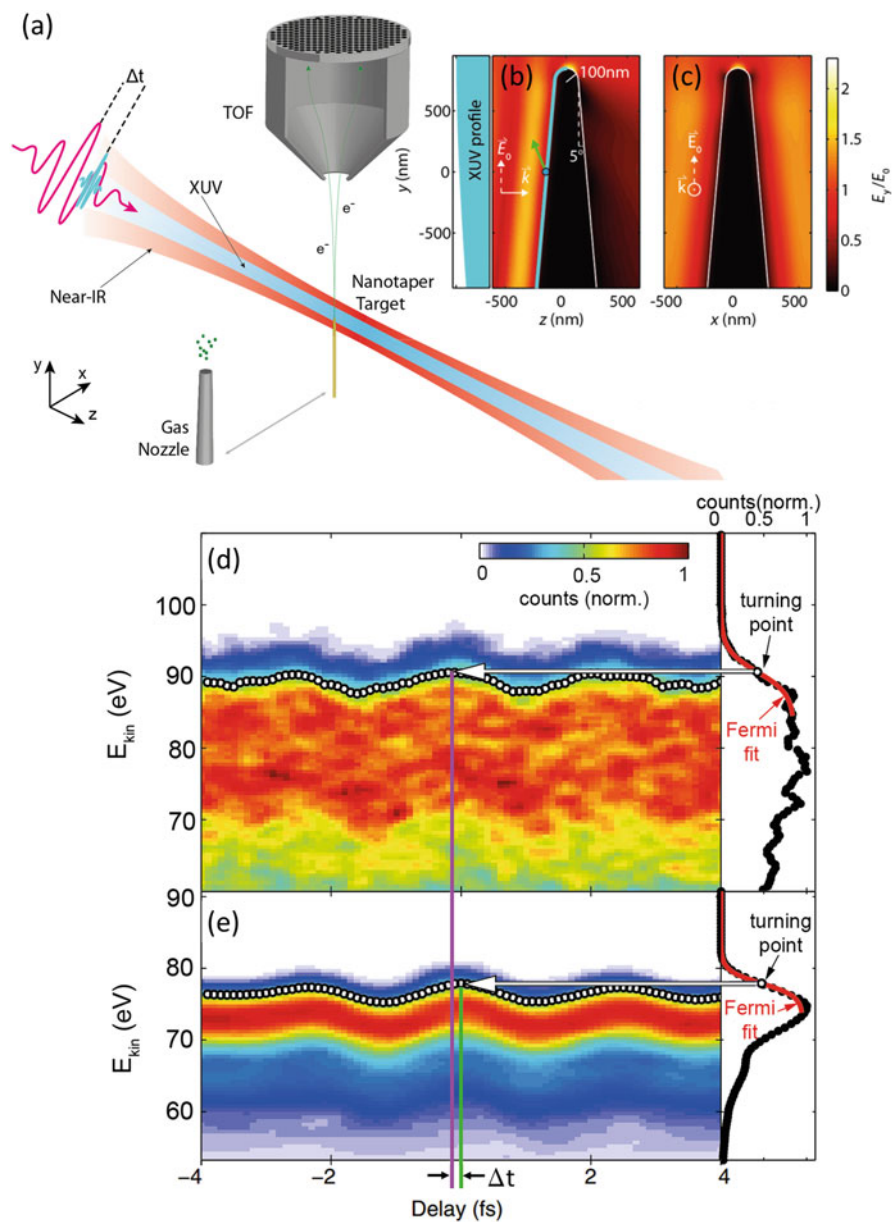


Fig. 14.9 (a) Schematic of experimental setup for attosecond nanoplasmonic near-field sampling. Isolated attosecond XUV and few-cycle NIR pulses are focused onto an Au nanotaper. For gas-phase reference measurements in Ne the taper is replaced by a gas nozzle. The electron emission is

centered at 720 nm excite collective electron dynamics in the nanotaper, resulting in spatially-varying near-fields (Fig. 14.9b, c). Delayed attosecond XUV pulses (220 as duration at 95 eV central photon energy) release electrons from the sample, which are subsequently accelerated by the near-fields. The tips were fabricated by electrochemical etching [42]. The delay-dependent momentum distribution of the emitted electrons is recorded with a TOF spectrometer aligned parallel to the laser polarization. For independent characterization of the incident NIR field and the XUV pulse by means of standard attosecond streaking, the taper can be replaced by a gas target (Ne). Neglecting the absolute photoemission time delay from Ne atoms, the gas phase streaking gives access to the vector potential of the incident NIR field.

Typical streaking spectrograms obtained from the Au nanotaper and Ne gas for the same laser parameters are presented in Fig. 14.9d and e, respectively. The panel to the right depicts the spectrum at a fixed delay. The high-energy edge of the Au spectrum is assigned to the photoemission of 5d electrons. For each time delay the high-energy part of the spectra was fitted with a Fermi function and from these fits the streaking curve was obtained (open circles in Fig. 14.9d, e). A relative shift between the streaking traces for tip and Ne is clearly visible, and is evaluated by fitting the streaking traces as $\Delta t = (200 \pm 50)$ as. In contrast to the previous attosecond studies on metal surfaces [25–27], where the streaking field component perpendicular to the surface was probed, in the presented experiment the field component parallel to the surface is probed. The decay of this field component inside the material is given by the skin depth (~ 30 nm) and is much larger than the XUV photoemission depth (~ 1 nm). It is therefore safe to assume that the delays due to the transport of the electrons to the surface are negligible in our experiments, and the shift is thus mostly attributed to the collective free-electron polarization response of the gold nanowire. The comparison with trajectory simulations in near-fields obtained with the macroscopic Maxwell's equations places the experiment in the ponderomotive streaking regime and provides access to the temporal evolution of the electric near fields around the nanotaper.



Fig. 14.9 (continued) detected by a TOF spectrometer at different relative delays of the XUV and NIR pulses. **(b, c)** Maximal normalized local field strengths of the electrical field component parallel to the taper axis in the plane of the laser propagation direction **(b)** and in the plane perpendicular to the laser propagation direction **(c)** as obtained from FDTD-simulations. The *green arrow* shows the maximum electron detection angle. The *blue* lineout illustrates the XUV photoemission area. **(d, e)** Experimental spectrograms obtained from measurements of the Au nanotaper **(d)** and Ne gas **(e)**. The *right* hand panels of the spectrograms show electron spectra for a fixed delay of -0.2 fs (nanotaper) and 0 fs (gas) illustrating extraction of the streaking curves. A Fermi function (*red*) is fitted to the cut-off edge of the spectrum. The turning points of the Fermi functions for different delay times provide the curves depicted by open circles in **(d)** and **(e)**

In summary, with a streaking approach our experiment allowed the complete temporal characterization of near-fields at nanostructures for the first time. Given the universality of the technique, we anticipate that it will help to understand and tailor collective electron dynamics on the nanoscale.

Acknowledgements We are grateful for support from our collaborators and colleagues that contributed to the presented work. We acknowledge funding by the DFG via SPP1840 (QUTIF), SPP1391, LMUexcellent and the center of excellence “Munich Centre for Advanced Photonics” and by the EU via the ERC grants “ATTOCO” (no. 307203) and “Near Field Atto” (no. 616823).

References

1. Zherebtsov, S., et al. (2011). Controlled near-field enhanced electron acceleration from dielectric nanospheres with intense few-cycle laser fields. *Nature Physics*, 7, 656.
2. Zherebtsov, S., et al. (2012). Carrier-envelope phase-tagged imaging of the controlled electron acceleration from SiO₂ nanospheres in intense few-cycle laser fields. *New Journal of Physics*, 14, 075010.
3. Ahmad, I., et al. (2009). Frontend light source for short-pulse pumped OPCPA system. *Applied Physics B: Lasers and Optics*, 97(3), 529–536.
4. Wittmann, T., et al. (2009). Single-shot carrier-envelope phase measurement of few-cycle laser pulses. *Nature Physics*, 5, 357–362.
5. Rathje, T., et al. (2012). Review of attosecond resolved measurement and control via carrier-envelope phase tagging with above-threshold ionization. *Journal of Physics B: Atomic, Molecular and Optical Physics*, 45, 074003.
6. Süßmann, F., et al. (2011). Single-shot velocity-map imaging of attosecond light-field control at kilohertz rate. *The Review of Scientific Instruments*, 82, 093109.
7. Stöber, W., Fink, A., & Bohn, E. (1968). Controlled growth of monodisperse silica spheres in the micron size range. *Journal of Colloid and Interface Science*, 26, 62.
8. Sau, T. K., & Murphy, C. J. (2004). Room temperature, high-yield synthesis of multiple shapes of gold nanoparticles in aqueous solution. *Journal of the American Chemical Society*, 126(28), 8648–8649.
9. Süßmann, F. (2013). *Dissertation LMU Munich*.
10. Süßmann, F., et al. (2015). Field propagation-induced directionality of carrier-envelope phase-controlled photoemission from nanospheres. *Nature Communications*, 6.
11. Seiffert, L., et al. (2015). Competition of single and double rescattering in the strong-field photoemission from dielectric nanospheres. *Applied Physics B: Lasers and Optics*, 122, 101.
12. Otobe, T., Yabana, K., & Iwata, J. I. (2009). First-principles calculation of the electron dynamics in crystalline SiO₂. *Journal of Physics: Condensed Matter*, 21(6), 064224.
13. Durach, M., et al. (2010). Metallization of nanofilms in strong adiabatic electric fields. *Physical Review Letters*, 105(8), 086803.
14. Stuart, B. C., et al. (1996). Nanosecond-to-femtosecond laser-induced breakdown in dielectrics. *Physical Review B*, 53(4), 1749–1761.
15. Gamaly, E. (2011). *Femtosecond laser-matter interactions: Theory, experiments and applications*. Singapore: Pan Stanford Publishing.
16. Lenzner, M., et al. (1998). Femtosecond optical breakdown in dielectrics. *Physical Review Letters*, 80(18), 4076–4079.
17. Schiffrin, A., et al. (2013). Optical-field-induced current in dielectrics. *Nature*, 493(7430), 70–74.
18. Dombi, P., et al. (2010). Observation of few-cycle, strong-field phenomena in surface plasmon fields. *Optics Express*, 18(23), 24206–24212.

19. Vogelsang, J., et al. (2015). Ultrafast electron emission from a sharp metal nanotaper driven by adiabatic nanofocusing of surface plasmons. *Nano Letters*, *15*(7), 4685–4691.
20. Hanke, T., et al. (2009). Efficient nonlinear light emission of single gold optical antennas driven by few-cycle near-infrared pulses. *Physical Review Letters*, *103*(25), 257404.
21. Anderson, A., et al. (2010). Few-femtosecond plasmon dephasing of a single metallic nanostructure from optical response function reconstruction by interferometric frequency resolved optical gating. *Nano Letters*, *10*(7), 2519–2524.
22. Rewitz, C., et al. (2012). Ultrafast plasmon propagation in nanowires characterized by far-field spectral interferometry. *Nano Letters*, *12*(1), 45–49.
23. Stockman, M. I., et al. (2007). Attosecond nanoplasmonic-field microscope. *Nature Photonics*, *1*(9), 539–544.
24. Kienberger, R., et al. (2004). Atomic transient recorder. *Nature*, *427*(6977), 817–821.
25. Okell, W. A., et al. (2015). Temporal broadening of attosecond photoelectron wavepackets from solid surfaces. *Optica*, *2*(4), 383–387.
26. Cavalieri, A. L., et al. (2007). Attosecond spectroscopy in condensed matter. *Nature*, *449*(7165), 1029–1032.
27. Neppel, S., et al. (2012). Attosecond time-resolved photoemission from core and valence states of magnesium. *Physical Review Letters*, *109*(8), 087401.
28. Skopalova, E., et al. (2011). Numerical simulation of attosecond nanoplasmonic streaking. *New Journal of Physics*, *13*, 083003.
29. Kelkensberg, F., Koenderink, A. F., & Vrakking, M. J. J. (2012). Attosecond streaking in a nano-plasmonic field. *New Journal of Physics*, *14*, 093034.
30. Hansen, P. M., et al. (2005). Expanding the optical trapping range of gold nanoparticles. *Nano Letters*, *5*(10), 1937–1942.
31. Süßmann, F., & Kling, M. F. (2011). Attosecond nanoplasmonic streaking of localized fields near metal nanospheres. *Physical Review B*, *84*, 121406(R).
32. Schenk, M., Kruger, M., & Hommelhoff, P. (2010). Strong-field above-threshold photoemission from sharp metal tips. *Physical Review Letters*, *105*(25), 257601.
33. Bormann, R., et al. (2010). Tip-enhanced strong-field photoemission. *Physical Review Letters*, *105*(14), 147601.
34. Krüger, M., Schenk, M., & Hommelhoff, P. (2011). Attosecond control of electrons emitted from a nanoscale metal tip. *Nature*, *475*(7354), 78–81.
35. Herink, G., et al. (2012). Field-driven photoemission from nanostructures quenches the quiver motion. *Nature*, *483*(7388), 190–193.
36. Piglosiewicz, B., et al. (2014). Carrier-envelope phase effects on the strong-field photoemission of electrons from metallic nanostructures. *Nature Photonics*, *8*(1), 37–42.
37. Yanagisawa, H., et al. (2009). Optical control of field-emission sites by femtosecond laser pulses. *Physical Review Letters*, *103*(25), 257603.
38. Thomas, S., et al. (2013). Probing of optical near-fields by electron rescattering on the 1 nm scale. *Nano Letters*, *13*(10), 4790–4794.
39. Park, D. J., et al. (2013). Characterizing the optical near-field in the vicinity of a sharp metallic nanoprobe by angle-resolved electron kinetic energy spectroscopy. *Annals of Physics (Berlin)*, *525*(1-2), 135–142.
40. Lienau, C., Raschke, M. B., & Ropers, C. (2015). *Ultrafast nano-focusing for imaging and spectroscopy with electrons and Light, in attosecond nanophysics: From basic science to applications* (pp. 281–324). Weinheim: Wiley-VCH.
41. Förg, B., et al. (2016). Attosecond nanoscale near-field sampling. *Nature Communications*, *7*, 11717.
42. Eisele, M., et al. (2011). Note: Production of sharp gold tips with high surface quality. *The Review of Scientific Instruments*, *82*(2), 026101.